Electronic structure of FeO, γ-Fe_2O_3, and Fe_3O_4 epitaxial films using high-energy spectroscopies

Juan Rubio-Zuazo,[1,2] Ashish Chainani,[3,4] Munetaka Taguchi,[3,5] Daniel Malterre,[6] Aida Serrano,[1,2] and German R. Castro[1,2]

[1]*Spanish CRG BM25-SpLine Beamline at the ESRF, 71 avenue des Martyrs 38000 Grenoble, France and ESRF-The European Synchrotron CS 40220, 38043 Grenoble Cedex 09, France*

[2]*Instituto de Ciencia de Materiales de Madrid-ICMM/CSIC, Cantoblanco, E-28049 Madrid, Spain*

[3]*RIKEN SPring-8 Center, 1-1-1 Sayo-cho, Hyogo 679-5148, Japan*

[4]*Condensed Matter Physics Group, National Synchrotron Radiation Research Center, Hsinchu 30076, Taiwan, R.O.C.*

[5]*Nara Institute of Science and Technology (NAIST), Ikoma, Nara, 630-0192, Japan*

[6]*Institut Jean Lamour, Universite de Lorraine, UMR 7198 CNRS, BP 70239, 54506 Vandoeuvre les Nancy, France*

(Received 26 March 2018; published 27 June 2018)

We study the electronic structure of well-characterized epitaxial films of FeO (wustite), γ-Fe_2O_3 (maghemite), and Fe_3O_4 (magnetite) using hard x-ray photoelectron spectroscopy (HAXPES), x-ray absorption near-edge spectroscopy (XANES), and electron energy loss spectroscopy (EELS). We carry out HAXPES with incident photon energies of 12 and 15 keV in order to probe the bulk-sensitive Fe 1*s* and Fe 2*p* core level spectra. Fe *K*-edge XANES is used to characterize and confirm the Fe valence states of FeO, γ-Fe_2O_3, and Fe_3O_4 films. EELS is used to identify the bulk plasmon loss features. A comparison of HAXPES results with model calculations for an MO_6 cluster provides us with microscopic electronic structure parameters such as the onsite Coulomb energy U_{dd}, the charge-transfer energy Δ, and the metal-ligand hybridization strength V. The results also provide estimates for the ground-state and final-state contributions in terms of the d^n, $d^{n+1}\underline{L}^1$, and $d^{n+2}\underline{L}^2$ configurations. Both FeO and γ-Fe_2O_3 can be described as charge-transfer insulators in the Zaanen-Sawatzky-Allen picture with $U_{dd} > \Delta$, consistent with earlier work. However, the MO_6 cluster calculations do not reproduce an extra satellite observed in Fe 1*s* spectra of γ-Fe_2O_3 and Fe_3O_4. Based on simplified calculations using an M_2O_7 cluster with renormalized parameters, it is suggested that nonlocal screening plays an important role in explaining the two satellites observed in the Fe 1*s* core level HAXPES spectra of γ-Fe_2O_3 and Fe_3O_4.

DOI: 10.1103/PhysRevB.97.235148

I. INTRODUCTION

Iron metal has the ability to form a wide variety of oxides with completely different physical and chemical properties [1,2]. Among them, FeO (wustite, or iron monoxide), with formally divalent Fe^{2+} ions, is paramagnetic at room temperature and becomes antiferromagnetic at low temperatures below $T_N = 198$ K [3]. It crystallizes in the rocksalt structure and lies in the middle of the MO series (M = Cr-Cu), famously discussed in terms of Mott-Hubbard insulators [4]. In contrast, γ-Fe_2O_3 (maghemite, or γ-iron-sesquioxide) is formally trivalent with only Fe^{3+} ions and forms in the inverse spinel structure [5]. It is a ferrimagnetic insulator at room temperature with a high ferrimagnetic ordering temperature of $T_C = 950$ K [5]. In contrast, α-Fe_2O_3 (hematite) is an antiferromagnetic insulator below $T_N = 260$ K, undergoing the Morin transition from a rhombohedral to trigonal structure at T_N [6]. Fe_3O_4 exhibits the well-known Verwey metal-insulator transition and is actually the first magnet known to mankind [7]. The reader is referred to an excellent recent review on the structure, as well as physical and chemical properties of the iron oxides and their surfaces [2].

It is well known that thin films of the iron oxides FeO, Fe_3O_4, and γ-Fe_2O_3 can be grown by pulsed laser deposition using the same starting target material, magnetite (Fe_3O_4), using different substrate temperatures and O_2 partial pressure conditions or by simple thermal annealing in vacuum or oxygen atmosphere, respectively [2,5,8]. This property enables an easy switching between the oxides and highlights their applications in industrial devices. Among many applications of these oxides, it is now known that γ-Fe_2O_3 nanoparticles can be used in biomedicine as it is biocompatible and nontoxic [1,9]. Thin films of γ-Fe_2O_3 are chemically stable and considerably cheap to make, and was hence used for conventional magnetic recording media [2,5]. More recently, it is actively pursued as an electrode material for lithium batteries [1,10]. It was shown that three-dimensional mesostructured electrodes made of γ-Fe_2O_3 exhibit improved cycling and rate performance as well as a lower hysteresis voltage compared to previously reported values, thus making it a viable battery material [10]. For FeO, recent studies have shown that water-mediated proton hopping can occur on a FeO monolayer film via a novel mechanism without the dissociation of water molecules [11], and is thus important for several applications such as catalytic hydrogen evolution, photocatalytic dehydrogenation, hydrogen storage, etc. The properties of FeO also play a very important role in the stratification of the Earth's outer core and is a favorite material for studying phase transitions under pressure. While early studies [12] had shown a transition from rocksalt to NiAs structure with a concomitant insulator-to-metal transition under pressure of 96 GPa and $T = 800$ K, more recently, it has been shown [13] that at still higher pressure (240 GPa) and $T = 4000$ K, FeO transforms to a CsCl structure.

In order to understand these interesting properties, several theoretical and experimental studies have been carried out on the electronic structure of FeO but there are very few

studies on γ-Fe_2O_3. On the theoretical front, dynamical mean-field theory (DMFT) studies of FeO, using the local density approximation (LDA) [14] as well as the generalized gradient approximation (GGA) [15], have concluded that FeO is a Mott insulator. Also, the pressure-dependent insulator-to-metal transition is best described as an orbital selective transition with the t_{2g} bands becoming metallic while the e_g bands remain insulating. For γ-Fe_2O_3, there are no DMFT calculations yet, but GGA + U calculations concluded that γ-Fe_2O_3 is a charge-transfer insulator [16]. It is also important to consider the role of doping in driving the insulator-to-metal transition in these materials.

There have been several electron spectroscopy studies in the past addressing the electronic structure of FeO and α-Fe_2O_3 [17–21]. But, there are only two studies on γ-Fe_2O_3: one addresses the basic electronic structure [22] and the other study investigates the surface structure [23]. However, all earlier photoelectron spectroscopy studies on FeO and γ-Fe_2O_3 have been done using soft x rays. The resulting low kinetic energy (∼500–700 eV) of photoelectrons for core level spectra makes it very surface sensitive, with an estimated [24] inelastic mean-free path (IMFP), $\lambda \sim 10$ Å. While electronic structure parameters for FeO and γ-Fe_2O_3 have been estimated by comparing the soft x-ray Fe $2p$ spectra with model cluster calculations, there has been no bulk-sensitive hard x-ray photoelectron spectroscopy (HAXPES; $h\nu = 6$–15 keV) studies to date on FeO and γ-Fe_2O_3. HAXPES has developed as an indispensable to study the bulk-sensitive electronic structure of solids [25–29]. Very recently, Miedema *et al.* studied α-Fe_2O_3 using HAXPES with $h\nu = 10$ keV [30] and model cluster calculations. It was shown that the Fe $1s$ core level HAXPES spectrum exhibits a main peak and two satellites, while the Fe $2p$ spectrum showed only one satellite. In fact, from a comparison of the Fe $1s$ and Fe $2p$ spectra, it was concluded that the second satellite in the Fe $2p_{3/2}$ spectrum was probably masked by the Fe $2p_{1/2}$ main peak, and hence Fe $1s$ photoemission is the best reference spectrum to obtain relevant electronic parameters. We discuss our results in comparison with the results of Miedema *et al.* in the following. Since ultrathin epitaxial films are important for device applications, we felt it would be useful to study well-characterized films of FeO, γ-Fe_2O_3, and Fe_3O_4 using high-energy spectroscopies and model cluster calculations and compare with earlier results discussed above. In addition, the cluster model calculations provide an estimate of the onsite Coulomb energy U_{dd}. Although U_{dd} is not the same as the Coulomb energy U used in LDA + U (local density approximation) band structure calculations, it can serve as a starting point for the calculations.

Hence, we have carried out HAXPES studies with incident photon energies of 12 and 15 keV in order to probe the bulk-sensitive (estimated $\lambda \sim 100$–150 Å) Fe $2p$ and Fe $1s$ core level spectra of FeO, γ-Fe_2O_3, and Fe_3O_4. We also report electron energy loss spectroscopy (EELS) spectra which help us to conclusively identify the bulk plasmon loss feature. A comparison of the HAXPES spectra with model MO_6 cluster calculations provides us with electronic structure parameters such as the onsite Coulomb energy U_{dd}, the charge-transfer energy Δ, and the metal-ligand hybridization strength V. U_{dd} is estimated to be ∼6–7 eV. This is similar to earlier estimates from cluster calculations [17,19,20,22], but larger than what has been often used ($U_{dd} \sim 4$–5 eV) in several band structure calculations [14,16,31,32]. Both FeO and γ-Fe_2O_3 can still be described as charge-transfer insulators in the Zaanen-Sawatzky-Allen picture with $U_{dd} > \Delta$. The ground-state configurations indicate that both FeO and γ-Fe_2O_3 have dominantly d^n contribution in the ground state, implying an ionic description due to the relatively low values of V, while the final states are dominated by the charge-transferred $d^{n+1}\underline{L}^1$ configuration. Further, the insulating phase of Fe_3O_4 can be simulated by a simple addition of FeO and γ-Fe_2O_3 spectra in a 1:1 ratio. However, an extra satellite seen in γ-Fe_2O_3 and Fe_3O_4 cannot be explained by MO_6 or MO_4 cluster calculations. Based on a simplified M_2O_7 cluster calculation and considering a renormalization of the energy levels, it is suggested that nonlocal screening plays an important role in explaining the two satellites observed in the Fe $1s$ core level HAXPES spectra of γ-Fe_2O_3 and Fe_3O_4.

II. EXPERIMENT

Thin films of FeO, Fe_3O_4, and γ-Fe_2O_3 were epitaxially grown on $SrTiO_3$(001) substrates by pulsed laser deposition using a Nd:YAG laser (wavelength: 355 nm) operating at 10 Hz and 1 J/cm^2 irradiance power. A stoichiometric polycrystalline Fe_3O_4 pellet was used as the target for growing the films. The FeO and γ-Fe_2O_3 thin film was deposited in an oxygen atmosphere of 2×10^{-7} and 1×10^{-4} mbar keeping the substrate temperature at 723 and 650 K, respectively. Fe_3O_4 films were obtained by depositing in an oxygen pressure of 9×10^{-7} mbar at 650-K substrate temperature. The formation of the desired oxide phases were monitored *in situ* by reflection high-energy electron diffraction (RHEED) using a primary electron energy of 29 keV. *Ex situ* grazing incidence x-ray diffraction (GIXRD) and x-ray absorption near-edge spectroscopy (XANES) measurements were carried out to confirm the desired single-phase character of the grown films.

A full GIXRD data analysis was carried out to demonstrate the single-phase character of the growth films. The substrate $SrTiO_3$ (STO) has a lattice parameter $a = 3.905$ Å (cubic). FeO grows fully relaxed with a bulk lattice parameter of 4.304 Å. In units of STO the (202) reflexion appears at $H = (3.905/4.304) * 2 = 1.814$ in an H scan. In the same way γ-Fe_2O_3 grows fully relaxed with a bulk lattice parameter 8.342 Å. In units of STO, the (404) reflexion appears at $H = (3.905/8.342) * 4 = 1.872$ for γ-Fe_2O_3 and $H = (3.905/8.398) * 4 = 1.86$ for Fe_3O_4 in the H scan. The presence of only the (202) reflection or the (404) reflections indicates the desired single phase of the films. Figure 1 shows representative GIXRD H scans taken at $K = 0$ and $L = 1.814$, 1.86, and 1.874 in STO reciprocal space units for FeO, Fe_3O_4, and γ-Fe_2O_3, respectively.

The thicknesses of the layers were obtained by low-angle reflectivity measurements which show clear fringes, as shown in Fig. 2. From the reflectivity data, we could estimate the thickness by fitting the reflectivity fringe positions, and the results indicate a thickness of ∼8 nm for the FeO film, ∼19 nm for the γ-Fe_2O_3 film, and ∼10 nm for the Fe_3O_4 film, respectively.

The XANES and HAXPES measurements were performed at the branches A and B of the BM25-SpLine beamline at

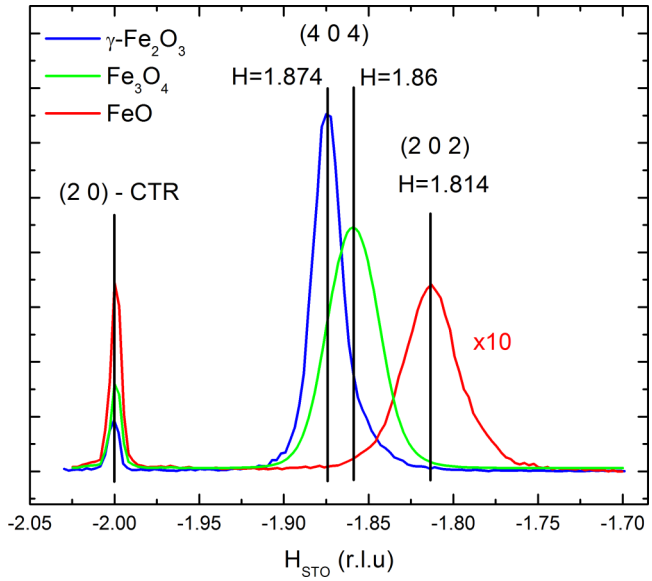

FIG. 1. X-ray diffraction of epitaxial thin films of FeO, γ-Fe_2O_3, and Fe_3O_4 films grown on $SrTiO_3$(001) substrates, obtained from crystal truncation rod (CTR) measurements. Note the presence of only the (202) reflection of FeO, or the (404) reflections of γ-Fe_2O_3 and Fe_3O_4 films, indicative of the desired single phase of the films.

the ESRF, respectively. The XANES experiments were also carried out on powder reference samples of FeO, γ-Fe_2O_3, and Fe_3O_4 (Sigma Aldrich). The phase purity of the powder samples was cross-checked by x-ray diffraction and they matched the known crystal structure of the compounds. The HAXPES measurements were done in the same experimental setup as the GIXRD measurements [33]. Photon energies of 12 and 15 keV were used to ensure accessibility to a wider reciprocal space region and for creating photoelectrons with high enough kinetic energies to probe the whole thickness

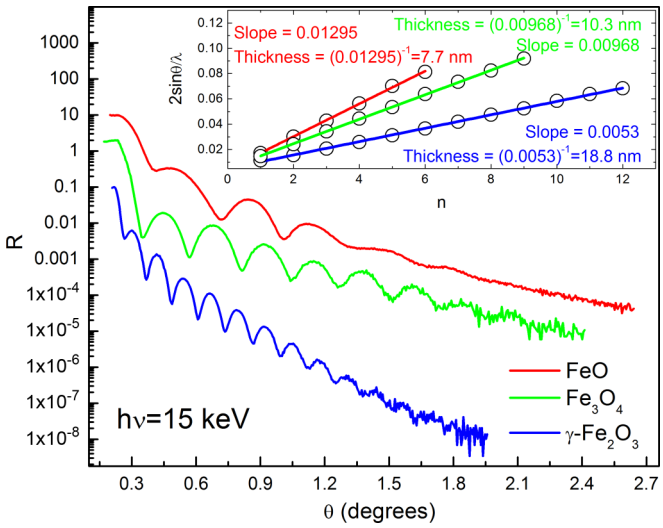

FIG. 2. X-ray reflectivity of epitaxial thin films of FeO, γ-Fe_2O_3, and Fe_3O_4 films grown on $SrTiO_3$(001) substrates. Inset shows the fit to the observed fringe positions for estimating the thickness of the films.

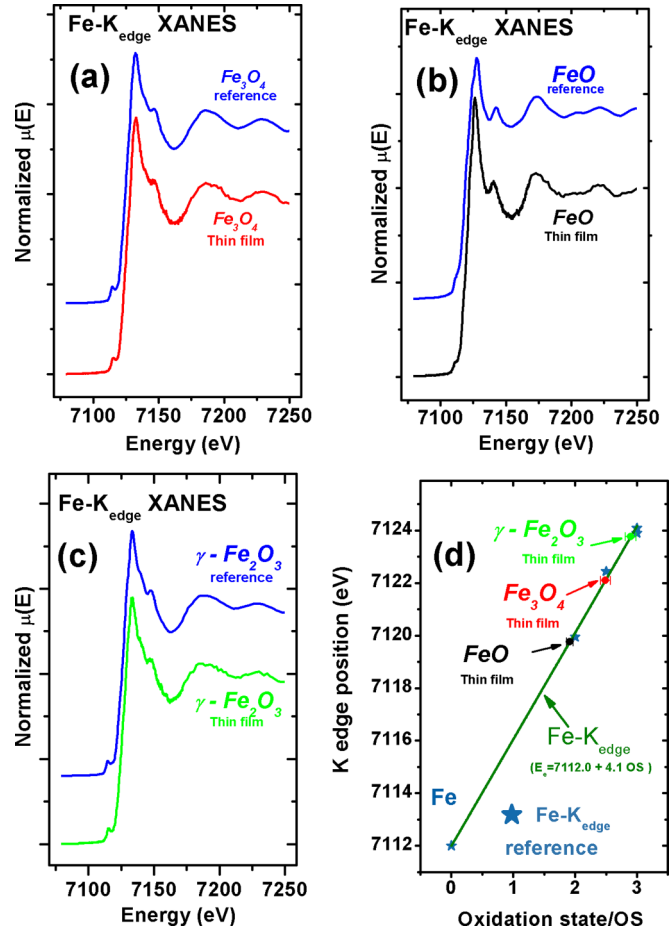

FIG. 3. XANES Fe K-edge spectra of Fe_3O_4 (a), FeO (b), and γ-Fe_2O_3 (c) epitaxial thin films and for comparison the corresponding reference spectra and the K-edge energy position of the films and references (d).

of the films. The HAXPES measurements were done using a Si(111) double-crystal monochromator (DCM) for $h\nu = 12$ keV and a second Si(004)DCM postmonochromator for $h\nu = 15$ keV, respectively. The energy resolution was 1.6 and 0.4 eV for HAXPES with $h\nu = 12$ and 15 keV. The EELS measurements were carried out with a primary electron beam energy of 7.9 keV corresponding to the Fe 1s photoelectron kinetic energy. All the measurements reported in this work were carried out in UHV (below 4×10^{-10} mbar). The spectra were calibrated using the Fermi level (E_F) measured from a copper sample holder.

III. RESULTS AND DISCUSSIONS

Figures 3(a)–3(c) show the XANES Fe K-edge spectra of Fe_3O_4, FeO, and γ-Fe_2O_3 thin films, respectively. In all the cases, we have measured powder samples as a reference, shown along with the spectra for the thin-film samples. The close similarity in all the spectroscopic features of the reference powder samples with thin-film data confirms the quality and the single-phase character of the films. Further, in Fig. 3(d), we plot the K-edge energy positions as a function of the valency or oxidation states and the results confirm the known linearity of

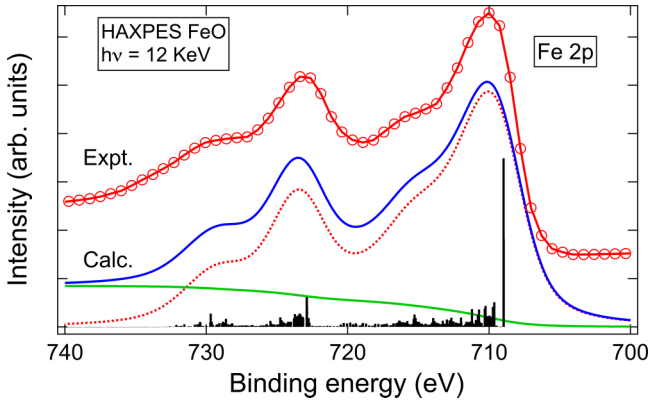

FIG. 4. Experimental and calculated HAXPES of Fe $2p$ core level of FeO thin film. Vertical lines are final-state contributions. The calculated spectrum is obtained by convolution of Voigt function.

the peak energy positions [34,35] with the nominal oxidation states of FeO, γ-Fe_2O_3, and Fe_3O_4.

Figure 4 shows the HAXPES Fe $2p$ core level spectrum of FeO and Fig. 5 shows the HAXPES Fe $2p$ core level spectrum of γ-Fe_2O_3, respectively, obtained using an incident photon energy of $h\nu = 12$ keV. The main Fe $2p_{3/2}$ peak of FeO is positioned at 710 eV while that for γ-Fe_2O_3 occurs at 710.5 eV binding energy. This is consistent with the soft x-ray Fe $2p$ spectra reported earlier [17–19,22,23,36,37]. In order to understand the origin of the features, we have carried out model cluster calculations for core level spectra based on the original work of Larsson [38] and of Van der Laan *et al.* [39]. The spectrum is calculated for a Fe^{2+} valence state using an FeO_6 cluster and the details of the method are described in Ref. [40]. For the initial and final states, we use a linear combination of the d^6, $d^7\underline{L}^1$, and $d^8\underline{L}^2$ states. The calculated results are shown in comparison with the experimental spectrum in Fig. 4. We plot the final-state contributions in the form of line diagrams, along with the total spectrum obtained by convolution with a Voigt function. The background shown in Fig. 4 (as well as in Figs. 5–8) was obtained as an integral of the corresponding experimental spectrum. We get a good match with the data for the following parameters: the onsite Coulomb

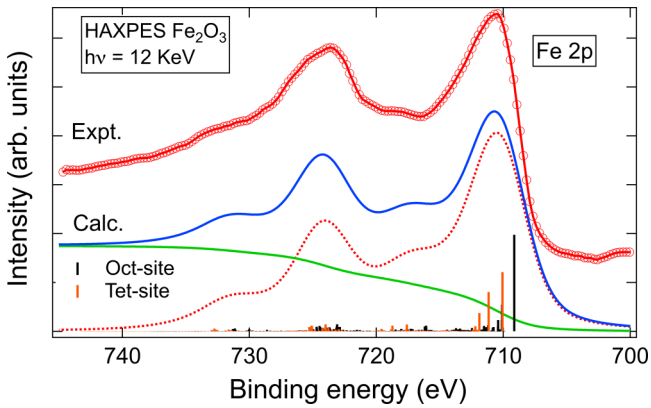

FIG. 5. Experimental and calculated HAXPES of Fe $2p$ core level of γ-Fe_2O_3 thin film. Vertical lines are final-state contributions. The calculated spectrum is obtained by convolution of Voigt function.

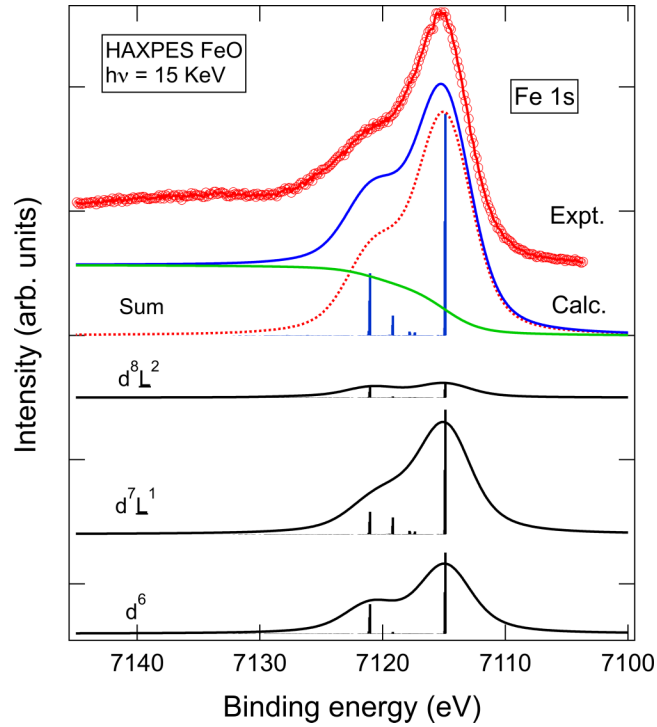

FIG. 6. Experimental and calculated HAXPES of Fe 1s core level of FeO thin film. Vertical lines correspond to the total and partial final state contributions.

energy $U_{dd} = 7.0$ eV, the charge-transfer energy $\Delta = 6.0$ eV, and the metal-ligand hybridization strength $V = 2.0$ eV. The crystal-field splitting between the t_{2g} and e_g states was set to 0.5 eV and the onsite Coulomb energy in the presence of a core hole $U_{dc} = 8.0$ eV. The crystal-field splitting value is taken from a very recent study which calculated the L-edge x-ray absorption spectrum (XAS) for FeO [41], while the U_{dc} is typically fixed to a value between 1.1 to 1.25*U_{dd}, as reported earlier [17–22]. The estimated parameters thus indicate that FeO is a charge-transfer insulator with U_{dd} being slightly larger than Δ.

As shown in Fig. 5, we carry out a similar analysis of the Fe $2p$ spectrum of γ-Fe_2O_3 using a Fe^{3+} valence state with d^5, $d^6\underline{L}^1$, and $d^7\underline{L}^2$ states. While FeO has a cubic rocksalt crystal structure, γ-Fe_2O_3 is a cubic inverse spinel with partial Fe vacancy ordering. This structural difference leads to an important difference for the local structure of Fe sites between the two systems: FeO has all Fe sites octahedrally coordinated to oxygen atoms while in γ-Fe_2O_3, the crystal has Fe sites in octahedral and tetrahedal coordination in a 5:3 ratio. Thus, for γ-Fe_2O_3, the calculations were done for both octahedral FeO_6 and tetrahedral FeO_4 clusters with the same parameters and the final spectrum was obtained by summing the two spectra in a 5:3 ratio, following the work of Fujii *et al.* [22]. We obtained a suitable match with the data for the following parameters: $U_{dd} = 6.0$ eV, $\Delta = 4.7$ eV, and $V = 2.3$ eV. The crystal-field splitting between the t_{2g} and e_g states was set to 0.9 eV and is based on an early study [20] which compared the XAS and resonant inelastic x-ray spectrum for α-Fe_2O_3, with calculations done by one of us. The onsite Coulomb energy in the presence of a core hole, $U_{dc} = 7.3$ eV, based on earlier

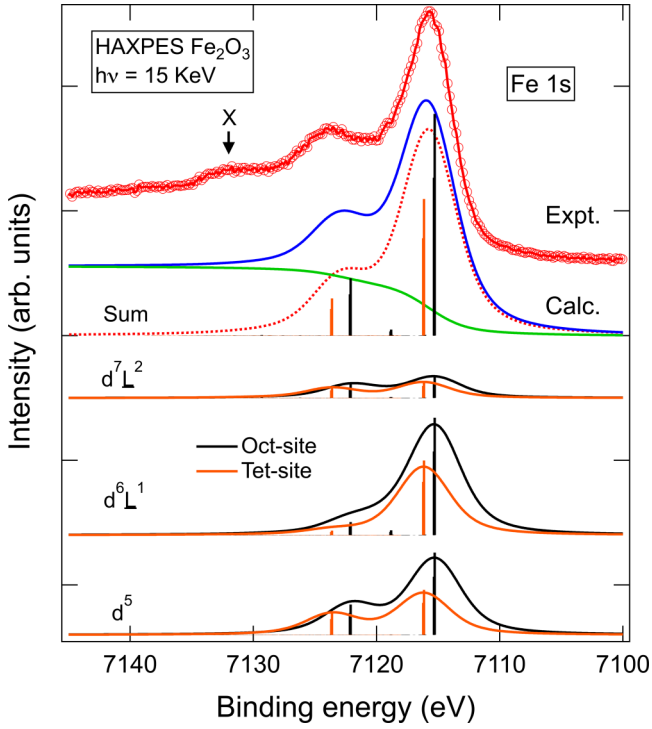

FIG. 7. Experimental and calculated HAXPES of Fe 1s core level of γ-Fe_2O_3 thin film. Vertical lines correspond to the total and partial final state contributions.

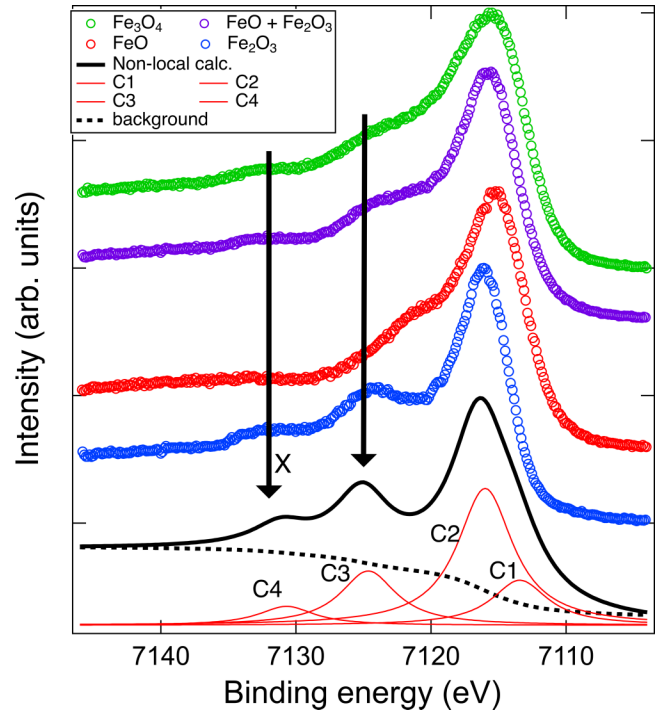

FIG. 8. HAXPES of Fe 1s core level of FeO, γ-Fe_2O_3, and Fe_3O_4 thin films, indicating the satellite structure originates from Fe^{3+}. A simple model calculation reproduces the satellite structure.

work [17–22]. The estimated parameters thus indicate that γ-Fe_2O_3 is also a charge-transfer insulator with U_{dd} being larger than Δ.

In Figs. 6 and 7, we discuss the HAXPES Fe 1s core level spectrum of FeO and γ-Fe_2O_3 thin films, respectively. Since the binding energies of the Fe 1s core levels are very high (∼7 keV), we decided to use an incident photon energy of hν = 15 keV so as to ensure a high kinetic energy and a bulk-sensitive measurement. The Fe 1s spectrum of FeO (Fig. 6) consists of a main peak lying at a binding energy of 7115 eV and a shoulder at about 7121.5 eV binding energy. The Fe 1s spectrum of γ-Fe_2O_3 (Fig. 7) consists of a main peak at a binding energy of about 7116 eV, but it shows two satellite features at about 7123.5 and 7132 eV binding energies. In Table I, we list the Fe 1s, Fe 2$p_{3/2}$, and Fe 2$p_{1/2}$ peak positions as well as the corresponding energy separation of the observed satellites from the main peaks of FeO, Fe_3O_4, and γ-Fe_2O_3, respectively. The calculated Fe 1s spectra of FeO and γ-Fe_2O_3 were obtained using the same set of parameters and procedures as for the Fe 2p spectra. Figures 6 and 7 also show the total calculated spectrum with the line diagrams for the final states for FeO and γ-Fe_2O_3, respectively.

While we could reproduce the Fe 1s spectrum of FeO, for γ-Fe_2O_3, we could reproduce only the main peak at 7116 eV and the first satellite (the so-called charge-transfer satellite) at 7123.5 eV binding energy. However, we could not reproduce the second satellite at a higher binding energy of 7132 eV (labeled X in Fig. 7) from the MO_6 cluster calculations. This result is similar to the case of the Fe 1s HAXPES spectrum of α-Fe_2O_3, which was reported recently using a photon energy of hν = 10 keV by Miedema *et al.* [30]. It is noted that earlier work [17,22] reporting soft x-ray Fe 2p photoemission of γ-Fe_2O_3 and α-Fe_2O_3 could not address this feature, which is seen clearly in the Fe 1s spectrum. In another recent study of a Mn d^5 system, Vobornik *et al.* [42] reported the Mn 1s core level HAXPES spectrum of $Bi_{0.91}Mn_{0.09}Te_3$ using a photon energy of 11 keV. The Mn 1s core level spectrum of $Bi_{0.91}Mn_{0.09}Te_3$ showed a main peak and a satellite at about 6 eV higher binding energy, which could be suitably reproduced by considering only the d^5 and d^6 states, following earlier work on Mn 2p HAXPES studies [43]. The authors

TABLE I. HAXPES Fe 1s and Fe 2$p_{2/3}$, and Fe 2$p_{1/2}$ binding energy (E_B) and the corresponding energy shift of the observed satellites (ΔS_1 and ΔS_2) of FeO, Fe_3O_4, and γ-Fe_2O_3, respectively.

	FeO		
Core level	E_B (eV)	ΔS_1 (eV)	ΔS_2 (eV)
Fe 1s	7115	6.5	
Fe 2$p_{3/2}$	710	5.8	
Fe 2$p_{1/2}$	723.6	7.2	
	Fe_3O_4		
Core level	E_B (eV)	ΔS_1 (eV)	ΔS_2 (eV)
Fe 1s	7115.1	8.0	16.5
Fe 2$p_{3/2}$	710.6		
Fe 2$p_{1/2}$	724.2	8.6	17.5
	Fe_2O_3		
Core level	E_B (eV)	ΔS_1 (eV)	ΔS_2 (eV)
Fe 1s	7116.1	7.6	15.9
Fe 2$p_{3/2}$	710.5	7.6	
Fe 2$p_{1/2}$	724.1	8.5	17.0

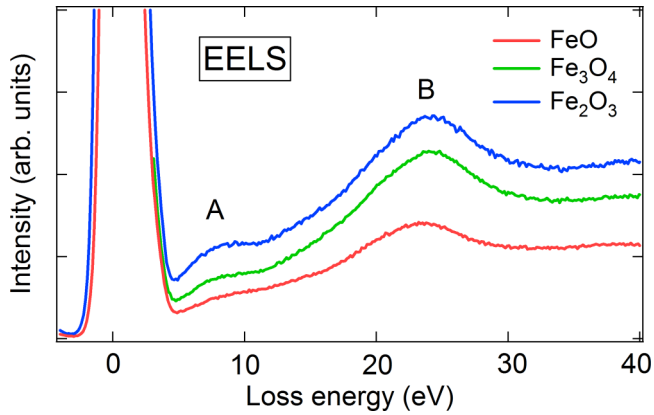

FIG. 9. EELS spectra of FeO, γ-Fe_2O_3, and γ-Fe_3O_4 epitaxial thin films.

also discussed the important difference between 1*s* and 2*p* core hole in terms of the degree of localization and screening, which affects the 3*d* electronic states.

In order to understand the discrepancy between our HAXPES experiments and the cluster calculation results, we first compared the Fe 1*s* spectra of FeO and γ-Fe_2O_3 with Fe_3O_4 thin films. Here, we note that, while bulk single-crystal Fe_3O_4 exhibits a Verwey transition at $T \sim 122$ K, it is known that films $\leqslant$25 nm in thickness do not exhibit the Verwey transition [44]. It was shown that thin films of $\leqslant$25 nm thickness are always insulating, from room temperature down to low temperatures [44]. In a recent study, it was reported that the Fe 2*p* spectra of Fe_3O_4 show a small but finite-temperature dependence in the Fe 2*p* spectra [45], but for the present insulating Fe_3O_4 films, the temperature dependence in Fe 2*p* and Fe 1*s* spectra are not expected as the film thickness is 10 nm. Figure 8 shows that the Fe_3O_4 Fe 1*s* HAXPES core level spectrum also exhibits an extra satellite at 7132.5 eV binding energy. Further, the Fe_3O_4 Fe 1*s* HAXPES core level spectrum can be well simulated by a simple addition of FeO and γ-Fe_2O_3 spectra in a 1:1 ratio, and the 7132.5 eV binding energy satellite matches fairly with the satellite observed in the γ-Fe_2O_3 spectrum at 7132 eV. This indicates that the extra satellite observed at about 7132 eV binding energy in γ-Fe_2O_3 and Fe_3O_4 orginates in the Fe^{3+} configuration.

Since plasmons can give rise to satellites at high binding energies in photoemission spectra, and it is well known that EELS is a suitable method to identify plasmon loss features [46], we carried out EELS of FeO, γ-Fe_2O_3, and Fe_3O_4 using a primary electron beam of 7.9 keV, to check for this possibility. As shown in Fig. 9, we plot the EELS spectra of FeO, γ-Fe_2O_3, and Fe_3O_4, respectively, with the zero of the energy scale corresponding to the primary energy of 7.9 keV. As can be seen from Fig. 9, FeO, γ-Fe_2O_3, and Fe_3O_4 spectra show a broad main loss feature (labeled B) centered at about 23–24 eV loss energy. In addition, the spectra also show a weak and broad feature centered at about 7.5 eV (labeled A). While there is no EELS calculation for γ-Fe_2O_3 and Fe_3O_4 to date, calculations [47] for the EELS spectrum of FeO based on the GGA $+U$ $+\Delta'$ method (where $U = 3$ eV is the onsite Coulomb energy, and $\Delta' = 1.5$ eV is the scissors shift used to account for the band gap) show a broad bulk plasmon loss feature between 19–24 eV, and weak features around 5–10 eV. The calculations are quite consistent with the experimental results, specifically for the main peak B which corresponds to the bulk plasmon. By analogy, we assign the peak centered at 23–24 eV for γ-Fe_2O_3 and Fe_3O_4 also to a bulk plasmon loss feature. In addition, since charge-transfer excitations can also be observed in EELS [48], the broad feature centered at about 7.5 eV is assigned to charge-transfer excitations. Thus, the weak high binding energy feature X at about 7132 eV in the Fe 1*s* photoelectron spectrum of γ-Fe_2O_3 and Fe_3O_4 (Figs. 7 and 8) cannot be assigned to a plasmon loss excitation.

TABLE II. Ground-state and final-state contributions obtained from analysis of the core level spectrum of FeO (Fe^{2+}) for the octahedral site.

Octahedral site configuration	Ground state	Final state
d^6	88.0%	35.8%
$d^7\underline{L}^1$	11.7%	54.8%
$d^8\underline{L}^2$	0.3%	9.4%

It is useful to discuss the ground-state and final-state contributions of FeO and γ-Fe_2O_3. In Table II, we list the ground-state and final-state contributions for FeO. As discussed earlier, the final-state contributions are plotted in Figs. 4 and 6 as line diagrams along with the spectra. It is found that the ground state is dominated by the d^6 configuration indicating a nearly ionic Fe^{2+}-like ground state, while the final states are dominated by the charge-transferred $d^7\underline{L}^1$ configuration. In Table III, we plot the ground-state and final-state contributions for the octahedral and tetrahedral sites of γ-Fe_2O_3. The final-state contributions are plotted in Figs. 5 and 7 as line diagrams along with the spectra. For γ-Fe_2O_3, the ground state is dominated by the d^5 configuration indicating a nearly ionic Fe^{3+}-like ground state, while the final states are dominated by the charge-transferred $d^6\underline{L}^1$ configuration. This behavior, of an ionic ground state for a charge-transfer system, is actually known from early work on Cu and Ni compounds [39,49], which showed that for relatively small hybridization strength V compared to U_{dd} and Δ, the ground state will be close to the pure d^n configuration even for charge-transfer insulators.

TABLE III. Ground-state and final-state contributions obtained from analysis of the core level spectrum of γ-Fe_2O_3 (Fe^{3+}) for the octahedral and tetrahedral sites.

Octahedral site configuration	Ground state	Final state
d^5	82.8%	38.8%
$d^6\underline{L}^1$	16.5%	48.0%
$d^7\underline{L}^2$	0.7%	13.2%
Tetrahedral site configuration	Ground state	Final state
d^5	77.7%	38.4%
$d^6\underline{L}^1$	21.1%	45.4%
$d^7\underline{L}^2$	1.2%	16.2%

The parameter set used by us is very similar to that used by Lee and Oh for analyzing soft x-ray Fe $2p$ spectrum of FeO, leading to a very similar d-electron count for the ground state [18]. Further, for γ-Fe_2O_3, the parameter values we have used for calculating the HAXPES spectra are very similar to the earlier study [20] of high-energy Fe K-edge XANES and the $1s$-$2p$ resonant inelastic x-ray scattering (RIXS) of α-Fe_2O_3. In that study, it was shown that the large Δ and a crystal-field splitting 10 Dq = 0.9 eV was important for obtaining the best match to the overall RIXS spectral shapes as a function of incident photon energy as well as the fine features of the pre-edge in Fe K-edge XANES. In comparison, Miedema *et al.* use a smaller $\Delta = 2$ or 3 eV, and a comparable $V_{eg} = 2.6$ eV for α-Fe_2O_3 and obtain a strong contribution from charge-transferred states even for the ground state [30]. While they obtain a highly reduced intensity for the high-energy satellite in their calculations when compared to the experimental data, they characterize it also as a charge-transfer satellite. Thus, it is clear that octahedral FeO_6 and tetrahedral FeO_4 cluster calculations with full atomic multiplets cannot reproduce the second satellite at high binding energy ($\sim$16 eV) from the main peak. We have instead tried an extremely simplified, or a toy model calculation, based on an M_2O_7 cluster which includes nonlocal screening [50–52] for explaining the extra satellite in the Fe $1s$ spectra. The importance of nonlocal screening stems from the fact that the core hole has an additional screening channel from the neighboring plaquette/cluster and was shown to be useful for understanding the metal $2p$ photoelectron spectra of NiO, cuprates, ruthenates, and manganites [50–52]. We would like to emphasize that we carried out the simplest nonlocal calculation because the full problem of two metal sites with a d^5 electron configuration is beyond our scope. The aim was just to check if the high-energy satellite, about 16 eV from the main peak, can be simulated in a model including nonlocal screening. The calculation is based on an effective renormalization of the electronic parameters for an M_2O_7 cluster calculation carried out for d^9 electron (d^1 hole) configuration on both the metal sites and the details are discussed in the Appendix. In a charge-transfer insulator, since the charge-transfer energy and Coulomb energy are the main pertinent energy scales, it is possible to map calculations from a d^9 configuration to a d^n charge-transfer system by using renormalized parameters, as was illustrated by Zaanen and Sawatzky [53]. A similar calculation was recently reported by us for the case of a hole-doped cuprate [54]. The calculation results are shown in Fig. 8 (black line) together with the experimental data. We obtain a fair match between the calculations with the experimental Fe $1s$ spectra.

In particular, the calculations reproduce the main peak as well as the two satellites for the following renormalized parameter set: the onsite Coulomb energy $U_{ddr} = 8.0$ eV, the charge-transfer energy $\Delta_r = 1.0$ eV, the metal-ligand hybridization strength $V_r = 1.15$ eV, and the onsite Coulomb energy in the presence of a core hole, $U_{dcr} = 11.0$ eV. We have analyzed the nature of the spectral features and we find that it consists of mainly four components C1–C4 (Fig. 8). The main peak consists of two components C1 and C2. C1 is dominated by the local and nonlocal screened state $|d^{10}\underline{L}^1; d^{10}\underline{L}^1\rangle$, while C2 has nearly equal contribution from $|d^{10}\underline{L}^1; d^{10}\underline{L}^1\rangle$ and $|d^9; d^9\rangle$ with admixture from the locally screened $|\mathrm{d}^{10}\underline{L}^1; \mathrm{d}^9\rangle$ state. The first satellite at 7123.5 eV is dominated by $|d^9; d^9\rangle$ with admixture from $|d^9; d^{10}\underline{L}^1\rangle$ and the second satellite (X) at 7132 eV is dominated $|d^9; d^9\rangle$ state with admixture from the $|d^{10}\underline{L}^1; d^{10}\underline{L}^1\rangle$ state. The results suggest that nonlocal screening is important for explaining the observed spectral features, and the full problem of two metal sites with d^5 electron configurations in an M_2O_7 cluster will be successful in reproducing the Fe $1s$ spectra with two satellites. While nonlocal screening models have been used for explaining metal $2p$ core level photoemission spectra earlier (Refs. [50–52]), it has never been used for explaining metal $1s$ core level photoemission spectra earlier. We hope our results will motivate future theoretical work for calculating metal $1s$ core level spectra with nonlocal screening for a d^5 system in particular, and d^n systems in general.

Finally, we note that the estimated ground-state contributions suggest that electron doping in FeO and γ-Fe_2O_3 will produce carriers of mainly "d" character while hole doping will result in mainly "p"-type carriers, i.e., an effective electron-hole asymmetry upon doping. In contrast, the ground state of most binary and ternary oxides of Mn and Co, except for MnO, are dominated by the charge-transferred states [19,21,55–58]. Thus, if the ground state and final states are dominated by the charge-transferred states, the materials are not expected to show a strong electron-hole asymmetry upon doping. For MnO, which has the same formal d^5 configuration as trivalent γ-Fe_2O_3, a very similar conclusion regarding the doped carriers has been made by Saitoh *et al.* [57] from an analysis of the core level spectra. While we also infer this from an analysis of the core level spectra, very remarkably, a similar conclusion was also made very early by Morin [59] for electron- and hole-doped α-Fe_2O_3. Morin, based on an analysis of the electrical resistivity, Seebeck coefficient, and optical spectra, concluded that it was necessary to consider two types of bands for explaining the observed transport behavior, namely, the sp bands of oxygen and the d bands of iron.

IV. CONCLUSIONS

In conclusion, we have investigated the electronic structure of well-characterized thin films of FeO (wustite), γ-Fe_2O_3 (maghemite), and Fe_3O_4 (magnetite) using HAXPES, XANES, and EELS. The MO_6 cluster model calculations allow us to estimate electronic parameters and indicate both FeO and γ-Fe_2O_3 are well described as charge-transfer insulators in the Zaanen-Sawatzky-Allen picture with $U_{dd} > \Delta$. However, due to a relatively lower hybridization V compared to U_{dd} and Δ, the ground state is dominated by the d^n configuration with a nearly ionic ground state, while the final states are dominated by the charge-transferred $d^{n+1}\underline{L}^1$ configuration. The estimated ground-state contributions suggest that electron doping in FeO and γ-Fe_2O_3 will produce carriers of mainly d character while hole doping will result in mainly p-type carriers. Based on a simplified M_2O_7 model cluster calculation, it is suggested that nonlocal screening plays an important role in explaining the two satellites observed in the Fe $1s$ core level HAXPES spectra of γ-Fe_2O_3 and Fe_3O_4.

ACKNOWLEDGMENTS

The authors are grateful to the BM25-SpLine staff for their valuable technical support beyond their duties and for the financial support from the Spanish Ministry of Economy, Industry, and Competitiveness (MINECO) and The Spanish National Research Council (CSIC) under Project No. PIE 20106OE013. The ESRF, MINECO, and CSIC are acknowledged for provision of synchrotron radiation facilities. A.C. thanks the Ministry of Science and Technology of the Republic of China, Taiwan, for financially supporting this research under Project No. MOST 106-2112-M-213-001-MY2.

APPENDIX

In order to understand the possible origin of the second satellite seen in γ-Fe_2O_3 and Fe_3O_4 at a binding energy of 7132 eV (Figs. 7 and 8), we carried out simplified model calculations using an M_2O_7 cluster. At the outset, we would like to emphasize that calculations including nonlocal screening for the d^5 electron configuration corresponding to the Fe^{3+} case are beyond our scope. We carried out a calculation by considering the M_2O_7 cluster with the two metal atoms having a d^1 hole (or d^9 electron) configuration instead of the real system with a d^5 electron configuration. This was done to check if nonlocal screening effects has the possibility to give us two satellites, one at about 8 eV and the second one approximately 16 eV separated in energy from the main peak. The initial and final states for the M_2O_7 cluster are a combination of the d^n configurations with charge transfer on both sites and across the plaquettes, e.g., $|d^9;d^9\rangle$, $|d^9;d^{10}L^1\rangle$, $|d^{10}L^1;d^9\rangle$, etc. The nonlocal screening becomes important when the ligand screening from the neighboring plaquette screens the core hole created on the metal site in the first plaquette. In the following, we discuss the relevance of these calculations in terms of a renormalization of energy levels for the Fe^{3+} case. The calculated spectra shown in Fig. 8 show that it is possible to obtain the second satellite in fair agreement with the data. The results suggest that nonlocal screening can give rise to additional satellites at higher-energy scales of up to 16 eV from the main peak.

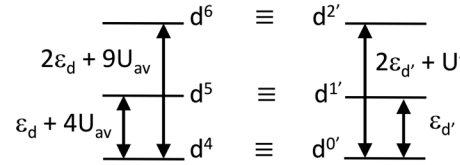

FIG. 10. Schematic to show the mapping of d^4, d^5, and d^6 states to $d^{0'}$, $d^{1'}$, and $d^{2'}$ states upon renormalization.

The renormalization of the energies for the d^5 case starting with the d^1 hole case is based on the following. For a given transition metal atom or ion, the average energies of the d^n configuration are given by $E^n_{av} = n\epsilon_d + n(n-1)U_{av}/2$ where ϵ_d is the one-electron energy and U_{av} is the Coulomb/exchange energy between pairs averaged over the multiplet states. For Fe^{3+}, the relevant d^n configuration is d^5 and we need to consider the energies of states with $n = 4$, 5, and 6.

Then, for $n = 4$, $E^4_{av} = 4\epsilon_d + 6U_{av}$, $n = 5$, $E^5_{av} = 5\epsilon_d + 10U_{av}$, $n = 6$, $E^6_5 = 6\epsilon_d + 15U_{av}$. It is possible to define renormalized parameters and to map the problem onto a simple $d^{0'}, d^{1'}$, and $d^{2'}$ problem. Consider for the renormalized system $\tilde{n} = 0'$ and $E^{0'}_{av} = E_{0'}$, $\tilde{n} = 1'$, and $E^{1'}_{av} = E_{0'} + \epsilon_{d'}$, $\tilde{n} = 2'$, and $E^{2'}_{av} = E_{0'} + 2\epsilon_{d'} + U'$.

The mapping $E^4_{av} \equiv E^{0'}_{av}$, $E^5_{av} \equiv E^{1'}_{av}$, and $E^6_{av} \equiv E^{2'}_{av}$ then $\Longrightarrow \epsilon_{d'} = E^5_{av} - E^4_{av} = \epsilon_d + 4U_{av}$ and $U' = E^{2'}_{av} - E^{0'}_{av} - 2\epsilon_{d'} = U_{av}$. Thus, the renormalization effectively corresponds to an energy shift of the $d^{0'}$, $d^{1'}$, and $d^{2'}$ energy levels and the levels are shown schematically in Fig. 10.

[1] P. Tartaj, M. P. Morales, T. Gonzalez-Carreno, S. Veintemillas-Verdaguer, and C. J. Serna, Adv. Mater. **23**, 5243 (2011).

[2] G. S. Parkinson, Surf. Sci. Rep. **71**, 272 (2016).

[3] C. A. McCammon, J. Magn. Magn. Mater. **104**, 1937 (1992); A. P. Kantor, S. D. Jacobsen, I. Yu. Kantor, L. S. Dubrovinsky, C. A. McCammon, H. J. Reichmann, and I. N. Goncharenko, Phys. Rev. Lett. **93**, 215502 (2004).

[4] N. F. Mott, Proc. Phys. Soc., London, Sect. A **62**, 416 (1949); L. F. Matheiss, Phys. Rev. B **5**, 290 (1972); **5**, 306 (1972); K. Terakura, A. R. Williams, T. Oguchi, and J. Kubler, Phys. Rev. Lett. **52**, 1830 (1984).

[5] R. Dronskowski, Adv. Funct. Mater. **11**, 27 (2001).

[6] L. Pauling and S. B. Hendricks, J. Am. Chem. Soc. **47**, 781 (1925); F. J. Morin, Phys. Rev. **78**, 819 (1950); P. Chen, N. Lee, S. McGill, S.-W. Cheong, and J. L. Musfeldt, Phys. Rev. B **85**, 174413 (2012).

[7] E. J. W. Verwey, Nature (London) **144**, 327 (1939).

[8] J. Rubio-Zuazo, L. Onandia, E. Salas-Colera, A. Muñoz-Noval, and G. R. Castro, J. Phys. Chem. C **119**, 1108 (2015); A. Muñoz-Noval, J. Rubio-Zuazo, E. Salas-Colera, A. Serrano, F. Rubio-Marcos, and G. R. Castro, Appl. Surf. Sci. **355**, 698 (2015).

[9] Q. A. Pankhurst, J. Conolly, S. K. Jones, and J. Dobson, J. Phys. D: Appl. Phys. **36**, R167 (2003).

[10] J. Wang, H. Zhou, J. Nanda, and P. V. Braun, Chem. Mater. **27**, 2803 (2015).

[11] L. R. Merte, G. Peng, R. Bechstein, F. Reiboldt, C. A. Farberow, L. C. Grabow, W. Kudernatsch, S. Wendt, E. Laegsgaard, M. Mavrikakis, and F. Besenbacher, Science **336**, 889 (2012).

[12] L. Fei and H. K. Mao, Science **266**, 1678 (1994).

[13] H. Ozawa, F. Takahashi, K. Hirose, and N. Hirao, Science **334**, 792 (2011).

[14] A. O. Shorikov, Z. V. Pchelkina, V. I. Anisimov, S. L. Skornyakov, and M. A. Korotin, Phys. Rev. B **82**, 195101 (2010).

[15] I. Leonov, Phys. Rev. B **92**, 085142 (2015).

[16] R. Grau-Crespo, A. Y. Al-Baitai, I. Saadoune, and N. H. De Leeuw, J. Phys.: Condens. Matter **22**, 255401 (2010).

[17] A. Fujimori, M. Saeki, N. Kimizuka, M. Taniguchi, and S. Suga, Phys. Rev. B **34**, 7318 (1986); A. Fujimori, N. Kimizuka, M. Taniguchi, and S. Suga, *ibid.* **36**, 6691 (1987).

[18] G. Lee and S. J. Oh, Phys. Rev. B **43**, 14674 (1991).

[19] A. E. Bocquet, T. Mizokawa, T. Saitoh, H. Namatame, and A. Fujimori, Phys. Rev. B **46**, 3771 (1992).

[20] W. A. Caliebe, C. C. Kao, J. B. Hastings, M. Taguchi, A. Kotani, T. Uozumi, and F. M. F. de Groot, Phys. Rev. B **58**, 13452 (1998).

[21] F. de Groot and A. Kotani, in *Core Level Spectroscopy of Solids, Advances in Condensed Matter Science*, edited by D. D. Sarma, G. Kotliar, and Y. Tokura (CRC Press, Boca Raton, FL, 2008), Vol. 6.

[22] T. Fujii, F. M. F. de Groot, G. A. Sawatzky, F. C. Voogt, T. Hibma, and K. Okada, Phys. Rev. B **59**, 3195 (1999).

[23] M. Bowker, G. Hutchings, P. R. Davies, D. Edwards, R. Davies, S. Shaikhutdinov, and H.-J. Freund, Surf. Sci. **606**, 1594 (2012).

[24] C. J. Powell and A. Jablonski, *NIST Electron Inelastic-Mean-Free-Path Database, Version 1.1* (National Institute of Standards and Technology, Gaithersburg, MD, 2000).

[25] K. Kobayashi *et al.*, Appl. Phys. Lett. **83**, 1005 (2003); Y. Takata *et al.*, *ibid.* **84**, 4310 (2004); C. Dallera *et al.*, *ibid.* **85**, 4532 (2004).

[26] C. S. Fadley, Nucl. Instrum. Methods, Phys. Res. Sect. A **601**, 8 (2009).

[27] L. Kövér, J. Electron Spectrosc. Relat. Phenom. **178**, 241 (2010).

[28] A. X. Gray, C. Papp, S. Ueda, B. Balke, Y. Yamashita, L. Plucinski, J. Minar, J. Braun, E. R. Ylvisaker, C. M. Schneider, W. Pickett, H. Ebert, K. Kobayashi, and C. S. Fadley, Nat. Mater. **10**, 759 (2011).

[29] *Hard X-ray Photoelectron Spectroscopy (HAXPES)*, edited by J. C. Woicik, Springer Series in Surface Sciences Vol. 59 (Springer, Switzerland, 2016).

[30] P. S. Miedema, F. Borgatti, F. Offi, G. Panaccione, and F. M. F. de Groot, J. Electron Spectrosc. Relat. Phenom. **203**, 8 (2015).

[31] A. Rohrbach, J. Hafner, and G. Kresse, Phys. Rev. B **70**, 125426 (2004).

[32] K. Pande, M. Gajdardziska-Josifovska, and M. Weinert, Phys. Rev. B **86**, 035431 (2012).

[33] J. Rubio-Zuazo and G. R. Castro, J. Electron Spectrosc. Relat. Phenom. **190**, 205 (2013); Nucl. Instrum. Methods Phys. Res., Sect. A **547**, 64 (2005).

[34] M. Abuin, A. Serrano, J. Chaboy, M. A. García, and N. Carmona, J. Anal. At. Spectrom. **28**, 1118 (2013).

[35] T. Nedoseykina, M. G. Kim, S.-A. Park, H.-S. Kim, S.-B. Kim, J. Cho, Y. Lee, Electrochim. Acta **55**, 8876 (2010).

[36] J. F. Moulder, W. F. Stickle, P. E. Sobol, and K. D. Bomben, *Handbook of X-ray Photoelectron Spectroscopy* (Physical Electronics, Eden Prairie, MN, 1995).

[37] F. Parmigiani and L. Sangaletti, J. Electron Spectrosc. Relat. Phenom. **98**, 287 (1999).

[38] S. Larsson, Chem. Phys. Lett. **40**, 362 (1976).

[39] G. van der Laan, C. Westra, C. Haas, and G. A. Sawatzky, Phys. Rev. B **23**, 4369 (1981).

[40] M. Taguchi, A. Chainani, N. Kamakura, K. Horiba, Y. Takata, M. Yabashi, K. Tamasaku, Y. Nishino, D. Miwa, T. Ishikawa, S. Shin, E. Ikenaga, T. Yokoya, K. Kobayashi, T. Mochiku, K. Hirata, and K. Motoya, Phys. Rev. B **71**, 155102 (2005).

[41] J. Luder, J. Schott, B. Brena, M. W. Haverkort, P. Thunstrom, O. Eriksson, B. Sanyal, I. Di Marco, and Y. O. Kvashnin, Phys. Rev. B **96**, 245131 (2017).

[42] I. Vobornik, G. Panaccione, J. Fujii, Z.-H. Zhu, F. Offi, B. R. Salles, F. Borgatti, P. Torelli, J. P. Pascal, D. Ceolin, A. Artioli, G. Levy, M. Marangolo, M. Eddrief, D. Krizmancic, H. Ji, A. Damascelli, G. van der Laan, R. G. Egdell, and R. J. Cava, J. Phys. Chem. C **118**, 12333 (2014).

[43] J. Fujii, M. Sperl, S. Ueda, K. Kobayashi, Y. Yamashita, M. Kobata, P. Torelli, F. Borgatti, M. Utz, C. S. Fadley, A. X. Gray, G. Monaco, C. H. Back, G. van der Laan, and G. Panaccione, Phys. Rev. Lett. **107**, 187203 (2011).

[44] W. Eerenstein, T. T. M. Palstra, T. Hibma, and S. Celotto, Phys. Rev. B **66**, 201101 (2002).

[45] M. Taguchi, A. Chainani, S. Ueda, M. Matsunami, Y. Ishida, R. Eguchi, S. Tsuda, Y. Takata, M. Yabashi, K. Tamasaku, Y. Nishino, T. Ishikawa, H. Daimon, S. Todo, H. Tanaka, M. Oura, Y. Senba, H. Ohashi, and S. Shin, Phys. Rev. Lett. **115**, 256405 (2015).

[46] F. Yubero and S. Tougaard, Phys. Rev. B **71**, 045414 (2005).

[47] C. Rodl and F. Bechstedt, Phys. Rev. B **86**, 235122 (2012).

[48] A. S. Moskvin, J. Málek, M. Knupfer, R. Neudert, J. Fink, R. Hayn, S.-L. Drechsler, N. Motoyama, H. Fisaki, and S. Uchida, Phys. Rev. Lett. **91**, 037001 (2003).

[49] J. Zaanen, C. Westra, and G. A. Sawatzky, Phys. Rev. B **33**, 8060 (1986).

[50] M. A. van Veenendaal, H. Eskes, and G. A. Sawatzky, Phys. Rev. B **47**, 11462 (1993); M. A. van Veenendaal and G. A. Sawatzky, *ibid.* **49**, 3473 (1994).

[51] K. Okada and A. Kotani, Phys. Rev. B **52**, 4794 (1995).

[52] M. van Veenendaal, Phys. Rev. B **74**, 085118 (2006).

[53] J. Zaanen and G. A. Sawatzky, Can. J. Phys. **65**, 1262 (1987).

[54] A. Chainani, M. Sicot, Y. Fagot-Revurat, G. Vasseur, J. Granet, B. Kierren, L. Moreau, M. Oura, A. Yamamoto, Y. Tokura, and D. Malterre, Phys. Rev. Lett. **119**, 057001 (2017).

[55] K. Okada and A. Kotani, J. Electron Spectrosc. Relat. Phenom. **58**, 325 (1992).

[56] J. C. Parlebas, M. A. Khan, T. Uozumi, K. Okada, and A. Kotani, J. Electron Spectrosc. Relat. Phenom. **71**, 117 (1995).

[57] T. Saitoh, A. E. Bocquet, T. Mizokawa, and A. Fujimori, Phys. Rev. B **52**, 7934 (1995).

[58] T. Uozumi, K. Okada, A. Kotani, R. Zimmermann, P. Steiner, S. Hufner, Y. Tezuka, and S. Shin, J. Electron Spectrosc. Relat. Phenom. **83**, 9 (1997).

[59] F. J. Morin, Phys. Rev. **83**, 1005 (1951); **93**, 1195 (1954).